



HAL
open science

Laser Actuated Microgripper Using Optimized Chevron-Shaped Actuator

Belal Ahmad, Hugo Chambon, Pierre Tissier, Aude Bolopion

► **To cite this version:**

Belal Ahmad, Hugo Chambon, Pierre Tissier, Aude Bolopion. Laser Actuated Microgripper Using Optimized Chevron-Shaped Actuator. *Micromachines*, 2021, 12 (12), pp.1487. 10.3390/mi12121487 . hal-03561332

HAL Id: hal-03561332


<https://hal.science/hal-03561332>

Submitted on 8 Feb 2022

HAL is a multi-disciplinary open access archive for the deposit and dissemination of scientific research documents, whether they are published or not. The documents may come from teaching and research institutions in France or abroad, or from public or private research centers.

L'archive ouverte pluridisciplinaire **HAL**, est destinée au dépôt et à la diffusion de documents scientifiques de niveau recherche, publiés ou non, émanant des établissements d'enseignement et de recherche français ou étrangers, des laboratoires publics ou privés.

Laser Actuated Microgripper using Optimized Chevron-shaped Actuator

Belal Ahmad ^{†,*} , Hugo Chambon [†], Pierre Tissier [†] and Aude Bolopion

FEMTO-ST Institute, Université Bourgogne Franche-Comté, CNRS, 25000 Besançon, France;

chambon.hugo@gmail.com (H.C.); pierre.tissier@icm-institute.org (P.T.); aude.bolopion@femto-st.fr (A.B.)

* Correspondence: belal.ahmad@femto-st.fr (B.A.)

† These authors contributed equally to this work.

Abstract: In this paper, we propose a laser actuated microgripper that can be activated remotely for micromanipulation applications. The gripper is based on an optothermally actuated polymeric chevron-shaped structure coated with optimized metallic layers to enhance its optical absorbance. Gold is used as a metallic layer due to its good absorption of visible light. The thermal deformation of the chevron-shaped actuator with metallic layers is first modeled to identify the parameters affecting its behavior. Then, an optimal thickness of the metallic layers that allows the largest possible deformation is obtained and compared with simulation results. Next, microgrippers are fabricated using conventional photolithography and metal deposition techniques for further characterization. The experiments show that the microgripper can realize an opening of 40 μm , a response time of 60 ms, and a generated force in the order of hundreds of μN . Finally, a pick-and-place experiment of 120 μm microbeads is conducted to confirm the performance of the microgripper. The remote actuation and the simple fabrication and actuation of the proposed microgripper makes it a highly promising candidate to be utilized as a mobile microrobot for lab-on-chip applications.

Keywords: Microgripper; Micromanipulation; Optothermal actuation

1. Introduction

The manipulation of micro-sized objects has drawn more attention in recent years to advance highly demanding domains such as microassembly and biomedicine [1–3]. Specifically, microgrippers are one of the widely used devices to handle microobjects [4–6]. At this scale, different actuation approaches, such as electric [7,8], thermal [9], magnetic [10] and optical [11], are used to control the motion of the microgripper, where piezoelectric and electrothermal actuation are most dominant in commercialized microgrippers. Because many microscale applications, especially biomedical applications, are conducted in closed environments, a remote actuation scheme is advantageous [12–14]. In fact, optothermal actuation, where light is utilized to generate heat at a specific location in an object, is one of the promising actuation approaches for microgrippers. Its remote and localized nature makes it a suitable candidate for mobile applications in closed environments [15]. Moreover, it allows simple integration of the microgripper in mobile microrobots, which are widely actuated by magnetic or acoustic fields, without affecting the actuation of the microrobot itself.

A number of works have utilized "the optothermal response to develop microactuators and microgrippers". In general, optothermal "microactuators and microgrippers are mainly implemented using smart material designs [16], or chevron-shaped actuators [17]. In smart material design, a photoresponsive material is mixed with a flexible material, e.g. polymers, to achieve a bending motion upon illumination [18]. These materials provide highly flexible motion that can be further controlled by patterning the

Citation: Lastname, F.; Lastname, F.; Lastname, F. Title. *Micromachines* **2021**, *1*, 0. <https://doi.org/>

Received:

Accepted:

Published:

Publisher's Note: MDPI stays neutral with regard to jurisdictional claims in published maps and institutional affiliations.

Copyright: © 2022 by the authors. Submitted to *Micromachines* for possible open access publication under the terms and conditions of the Creative Commons Attribution (CC BY) license (<https://creativecommons.org/licenses/by/4.0/>).

38 mixed material through advanced techniques such as shape programming [19]. Nonethe-
39 less, this comes at the cost of increased fabrication complexity. On the other hand, the
40 chevron-shaped actuators, which are commonly based on polymers and are fabricated
41 using conventional photolithographically techniques, offer an effective actuator that can
42 generate relatively large displacement without complex fabrication techniques, in con-
43 trast to smart materials. Although the flexibility and range of motion of chevron-shaped
44 actuators is lower than their smart materials counterparts, they offer a comparatively
45 high generated force, which is critical for micromanipulation [20]. For instance, Elbuken
46 et al. [17] have developed a photothermally actuated microgripper fabricated with a
47 single polymeric layer (SU-8) and based on a chevron-shaped actuator. The microgrip-
48 per could be actuated remotely to realize an opening of 30 μm using a focused laser
49 beam to heat up a connection spot between two beams in the chevron-shaped structure.
50 However, a common problem when utilizing the photothermic behavior of polymeric
51 actuators is their low optical absorbance [21], which drastically reduces the overall
52 displacement of such actuators. Because chevron-shaped actuators can be fabricated
53 with common microelectromechanical systems (MEMS) fabrication techniques, a viable
54 workaround is to use metallic coating to enhance the optical absorbance. By using a
55 metal with high optical absorbance, the overall deflection of the chevron-shaped actuator
56 can be increased. Moreover, the high absorbance of optical energy drastically enhances
57 the response speed of the actuator. Specifically, gold is a superior absorbent of visible
58 light and has shown high potential in optothermal actuation [22,23]. For example, gold
59 nanoparticles have been integrated in a tunable biopolymer material to facilitate its op-
60 tothermal response [24]. Moreover, gold is a commonly available material in cleanrooms
61 with a well know deposition processes. Still, the integration of gold in microactuators
62 increases its fabrication complexity. In this paper, we propose a polymeric microgripper
63 utilizing a gold metallic coated chevron-shaped actuator that can be actuated remotely
64 with a laser. Our aim is to overcome the low optical absorbance limitation of polymers
65 by introducing a gold metallic layer with optimal thickness that would not affect the
66 flexibility of the polymer itself. The thickness of the metallic layer is optimized to realize
67 the largest possible opening of the microgripper. By virtue of the metallic layer, the
68 proposed microgripper can realize large displacements and a fast response compared to
69 previously developed polymeric microgrippers. To our knowledge, this work is the first
70 attempt to enhance the optothermal actuation of chevron-shaped microgrippers using
71 metallic coating. The untethered nature of laser actuation makes it possible to integrate
72 the microgripper in a mobile microrobot in future work.

73 2. Microgripper Design, Optimization, and Fabrication

74 In this section, the microgripper design and the base material choice are first intro-
75 duced. Next, the metal-coated chevron-shaped actuator, which is the main component
76 of the microgripper, is optimized to realize relatively large deflections. Finally, the
77 fabrication process of the microgripper is shown.

78 2.1. Design of Microgripper

79 The main component of the proposed microgripper is a chevron-shaped thermal
80 actuator that produces translational displacement when heated. The two beams of the
81 actuator, called "chevron beams", are connected to the body of the microgripper from
82 one end, acting as a fixed end, and to a common connection point, called "chevron
83 shuttle", acting as a free end, as shown in Figure 1(a). It is worth noting that it is
84 possible to add more pairs of chevron beams to the design as will be shown in the
85 experimental section. Upon heating the chevron shuttle using a focused laser beam,
86 the heat is conducted through the chevron beams causing them to expand, creating a
87 translational displacement at the shuttle, as shown in Figure 1(b). This displacement is
88 utilized to push the fingers of the microgripper, which are normally in a closed state,
89 further apart achieving an open state. Specifically, the normally closed state allows

90 the microgripper to hold and move microobjects without being continuously heated
 91 by the laser beam, which is preferable to reduce the amount of heat dissipated in the
 92 surrounding environment.

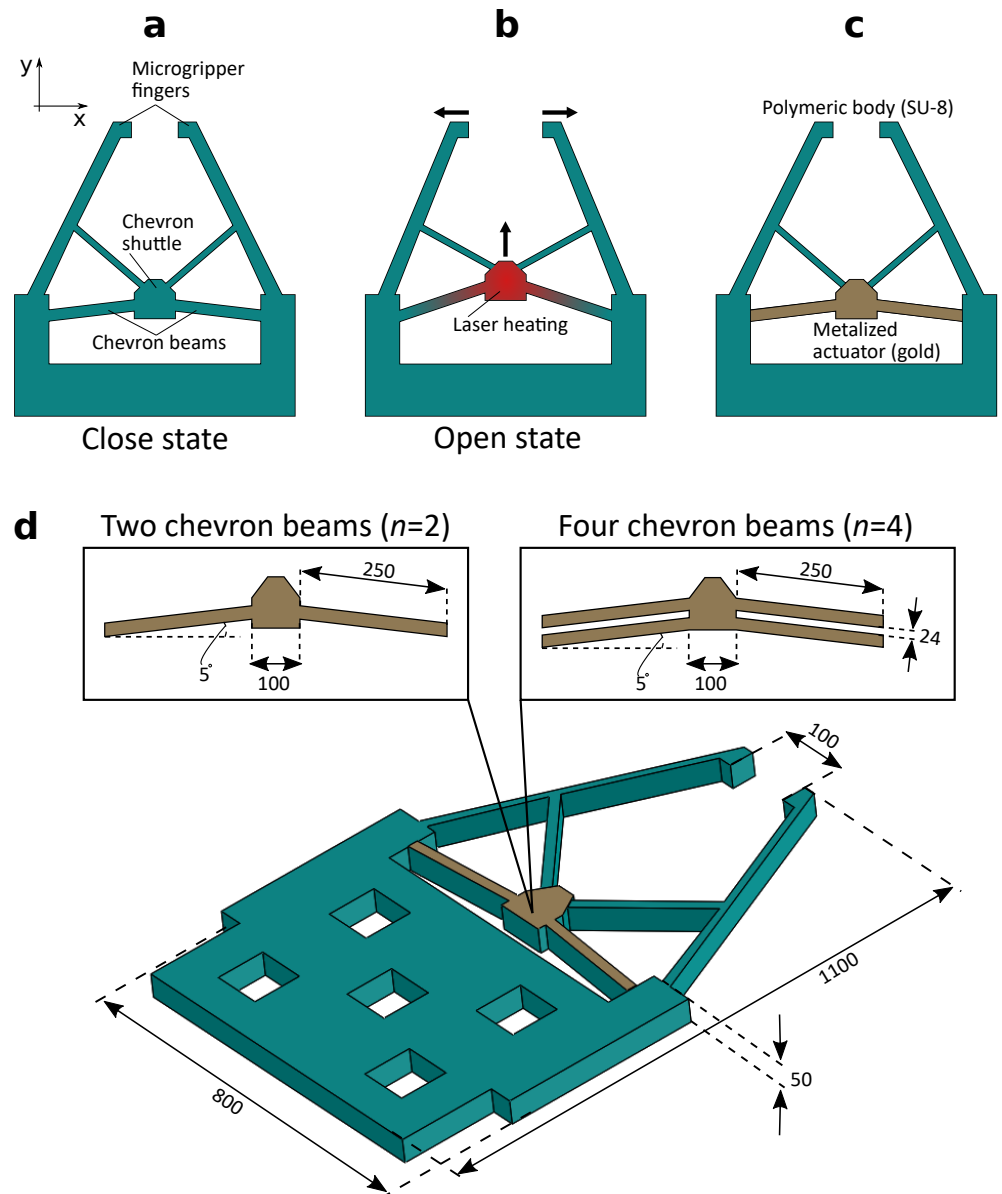


Figure 1. (a) Schematic of the proposed microgripper. (b) Laser heating of the chevron-shaped actuator results in opening the microgripper. (c) Material structure of the microgripper. (d) Dimensions of the microgripper. Two possible designs with two chevron beams ($n = 2$) and four chevron beams ($n = 4$) are shown. All dimensions are in μm .

93 The material structure of the microgripper is shown in Figure 1(c). SU-8 resin was
 94 chosen as the body material of the microgripper. The use of SU-8 offers a number of
 95 advantages in microfabrication and thermal actuation. Because SU-8 is a very common
 96 material in MEMS manufacturing, its fabrication process is straightforward and it can be
 97 deposited in a thick layer (several ten microns). In addition, SU-8 is known to produce
 98 relatively large displacements in response to temperature change owing to its high
 99 thermal expansion coefficient [25]. On the other hand, the use of SU-8 poses a number of
 100 disadvantages especially in the case of optothermal actuation. Specifically, the thermal
 101 conduction coefficient of SU-8 is low, which is both advantageous and disadvantageous.
 102 In fact, when heating the chevron-shaped actuator with a laser, the low thermal con-

duction coefficient of SU-8 drastically reduces the amount of heat conducted from the heated actuator to the fingers of the microgripper. This is advantageous in biomedical applications to prevent damage to the manipulated biological entities. However, the disadvantage is the low temperature conduction from the heated shuttle to the beams of the chevron-shaped actuator, which reduces its overall displacement. Moreover, the transparent nature of SU-8 drastically reduces its optical absorbance; thus reducing its deformation when heated using a laser beam.

To compensate for the transparency of SU-8 and to enhance its optical energy absorption, a thin layer of a high optical absorbance metal is selectively deposited on the chevron-shaped actuator. The metallic layers are deposited on both sides of the actuator with equal thicknesses to reduce the bimaterial effect. In fact, the thickness of the metallic layer is a key parameter to achieve the largest possible deflection. On the one hand, an excessively thick layer would increase the stiffness of the chevron-shaped actuator reducing its deflection. On the other hand, an excessively thin layer would suffer from low optical absorbance. Therefore, the thickness of the metallic layer should be optimized for maximal possible deflection. The full design and dimension of the microgripper are shown in Figure 1(d). The figure demonstrates the ability to vary the number of chevron beams through two examples of chevron actuators having two ($n = 2$), or four ($n = 4$) chevron beams.

2.2. Modeling and Optimization of Metal-coated Chevron-shaped Actuator

In order to optimize the design of the chevron-shaped actuator, a model should be first derived. Because the actuator is symmetrical on the yz -plane, a model of only half of the actuator cut in the yz -plane is derived for simplicity. A schematic of the deflection of a half chevron-shaped actuator upon heating is shown in Figure 2(a). The translational motion (δ) of the chevron shuttle can be estimated as a function of the variation in the length of the chevron beam (ΔL) as follows:

$$\delta = \sqrt{2L\Delta L + \Delta L^2 + L^2 \sin^2(\beta)} - L \sin(\beta) \quad (1)$$

$$\Delta L = \int_0^L T(x)\alpha dx \quad (2)$$

where L is the length of the chevron beam, β is the angle of the chevron beam with respect to the x -axis, $T(x)$ is the temperature of the cross section of the chevron beam located at x coordinate, and α is the thermal expansion coefficient. From the model, it can be confirmed that the deflection of the chevron shuttle (δ) increases with decreasing angle of the chevron beam (β). The temperature conduction along the chevron beam can be modeled similar to the heat transfer from a fin by assuming that the temperature is constant over a small length dx as shown in Figure 2(b). The temperature conduction should take into account the different thermal conductivity of the the SU-8 body and the two metallic layers. The two metallic layers have equal thicknesses ($e_{m1} = e_{m2} = e_m$).

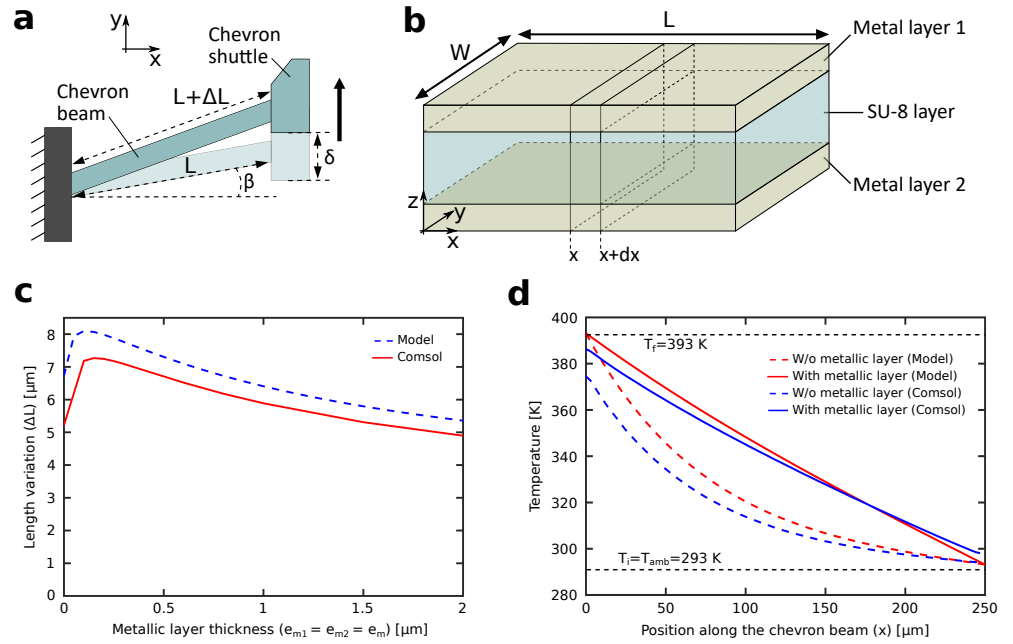


Figure 2. Modeling of the thermal deformation of a metal coated chevron-shaped actuator. (a) Schematic of the deflection of a half chevron-shaped actuator upon heating. (b) Sectional view of the chevron beam. (c) Effect of the thickness of the metallic layer on the length variation of the chevron beam. The blue dashed line and the red solid line show the model calculations and the simulation results, respectively. (d) Effect of adding metallic layers on the temperature gradient of the chevron actuator. The metallic layers thicknesses $e_{m1} = e_{m2} = e_m = 200$ nm. The red solid line and the red dashed line show the model calculations for the cases with and without metallic layers, respectively, and the blue line and the blue dashed line show the simulation results for the cases with and without metallic layers, respectively.

$$\frac{d^2T(x)}{dx^2} = h \frac{p}{\lambda A} (T(x) - T_{amb}) \quad (3)$$

139 where h is the heat transfer coefficient of air, λ is the thermal conductivity of the chevron
 140 beam material, p is the perimeter of the chevron beam cross-section, A is the area of the
 141 chevron beam cross-section, and T_{amb} is the ambient temperature. By substituting the
 142 geometrical parameters of the chevron beam and the two different thermal conductivities
 143 of SU-8 and the metallic layers in equation (3) we can get:

$$\frac{d^2T(x)}{dx^2} = h \frac{(2W + 4e_m + 2e_s)}{\lambda_s A_s + 2\lambda_m A_m} (T(x) - T_{amb}) \quad (4)$$

144 where λ_s , λ_m are the thermal conductivities of SU-8 and the metallic layers, respectively,
 145 e_s , e_m are the thicknesses of SU-8 and the metallic layers, respectively, W is the width of
 146 the chevron beam, and A_s , A_m are the areas of the cross sections of the SU-8 layer and
 147 the metallic layers, respectively. The solution for equation (4) gives us the temperature
 148 profile along the length of the chevron beam as follows:

$$T(x) = B \exp(Dx) + C \exp(-Dx) + T_{amb} \quad (5)$$

$$D = \sqrt{\frac{h(2W + 4e_m + 2e_s)}{\lambda_s A_s + 2\lambda_m A_m}}; \quad (6)$$

$$B = T_f - T_{amb} - \frac{T_i - T_{amb} + (T_{amb} - T_f) \exp(DL)}{\exp(-DL) - \exp(DL)}; \quad (7)$$

$$C = T_f - B - T_{amb} \quad (8)$$

149 where T_i , T_f are the initial and final temperatures of the chevron beam. Finally, the
150 length variation expressed in equation (2) can be rewritten as:

$$\Delta L = \int_0^L T(x) \alpha_{eq} dx = \frac{\alpha_{eq}}{D} (B \exp(DL) - C \exp(-DL) - (B - C)) \quad (9)$$

$$\alpha_{eq} = \frac{A_s E_s \alpha_s + 2A_m E_m \alpha_m}{A_s E_s + 2A_m E_m} \quad (10)$$

151 where E_s , E_m are the Young's moduli of SU-8 and the metallic layers, respectively, and
152 α_s , α_m are the thermal expansion coefficients of SU-8 and the metallic layers, respectively.
153 Equation (9) gives a relation between the parameters of the chevron-shaped actuator
154 and its thermally induced length variation. Therefore, the effect of the thickness of the
155 metallic layer on the length variation can be estimated, as shown in Figure 2(c). The
156 figure includes the model calculations based on equation (9), shown in the blue dashed
157 line, and the simulation results using Comsol shown in the red solid line. It can be
158 confirmed from the figure that an optimal value for the thickness of the metallic layer,
159 which can generate the maximum length variation of the chevron-beam, can be obtained.
160 This value was confirmed to be 200 nm and it will be used in subsequent sections. In
161 addition, the maximum opening of the microgripper can be controlled by varying the
162 metallic layer thickness, taking in mind that all other parameters affecting ΔL , such
163 as the dimensions of the chevron beams and the length of the microgripper's fingers,
164 are fixed. On the other hand, the temperature gradient along the chevron-beam can
165 be obtained using equation (5), as shown in Figure 2(d). The same equation can be
166 used to verify the effectiveness of the metallic layer by verifying the effect of adding
167 a metallic layer on the temperature gradient. Two cases of chevron beams with and
168 without metallic layers are shown. Here, the optimal value of 200 nm for the thickness
169 of metallic layer is used. The figure includes the model calculations based on equation
170 (5) for the cases with and without metallic layers, shown in the red solid line and red
171 dashed line, respectively, and the simulation results using Comsol for the cases with
172 and without metallic layers, shown in the blue line and blue dashed line, respectively.
173 In the case of no metallic layer, the temperature exponentially drops along the length
174 of the chevron-beam, which reduces its overall length variation. On the other hand, a
175 linear drop in temperature along the length of the chevron-beam can be confirmed after
176 adding metallic layer, which shows the advantage of adding an optimized metallic layer
177 to the chevron-shaped actuator.

178

179 2.3. Fabrication of Microgripper

180 The microgripper is fabricated using conventional photolithography and metal
181 deposition techniques. The process uses three different masks to construct the main
182 SU-8 body and metallic layers of the microgripper. The fabrication flowchart is shown in
183 Figure 3(a), and is described as follows: (1) an 800 nm sacrificial layer of aluminum (Al)
184 is deposited by sputtering on a silicon (Si) wafer. (2) a 350-nm thick layer of chromium
185 (Cr), a 200-nm thick layer of gold (Au), and a 45-nm thick layer of Cr are deposited
186 by sputtering, respectively. The chromium layers are added to enhance the adhesion
187 between metal-metal layers and metal-polymer layers. (3) the first photolithography
188 process using the first mask (mask A) is conducted with positive photoresist (S1813)

189 to shape the lower metallic layers. (4) wet etching of Cr followed by wet etching of
 190 Au are conducted for 30 sec and 2 min, respectively. (5) the photoresist is removed by
 191 acetone. (6) a 50 μm -thick layer of SU-8 is deposited using spin coating. Two-steps spin
 192 coating is used with speeds of 500 rpm for 30 sec and 2500 rpm for 30 sec, respectively.
 193 (7) the second photolithography process using the second mask (mask B) is conducted
 194 to shape the SU-8 layer. (8) a 45-nm thick layer of Cr and a 200-nm thick layer of Au are
 195 deposited by sputtering, respectively. (9) the third photolithography process using the
 196 third mask (mask C) is conducted with positive photoresist (S1813) to shape the upper
 197 metallic layers. It is worth noting that mask C is similar to mask A but with enlarged thin
 198 parts of the microgripper, such as the chevron beams, to simplify the alignment process.
 199 (10) wet etching of Au followed by wet etching of Cr are conducted for 2 min and 5
 200 min, respectively. (11) the photoresist is removed by acetone. (12) the microgrippers
 201 are released by wet etching of Al followed by wet etching of Cr. The etching times in this
 202 step were determined visually until the removal of the Al and Cr layers are confirmed.
 203 An example of a fabricated microgripper is shown in Figure 3(b).

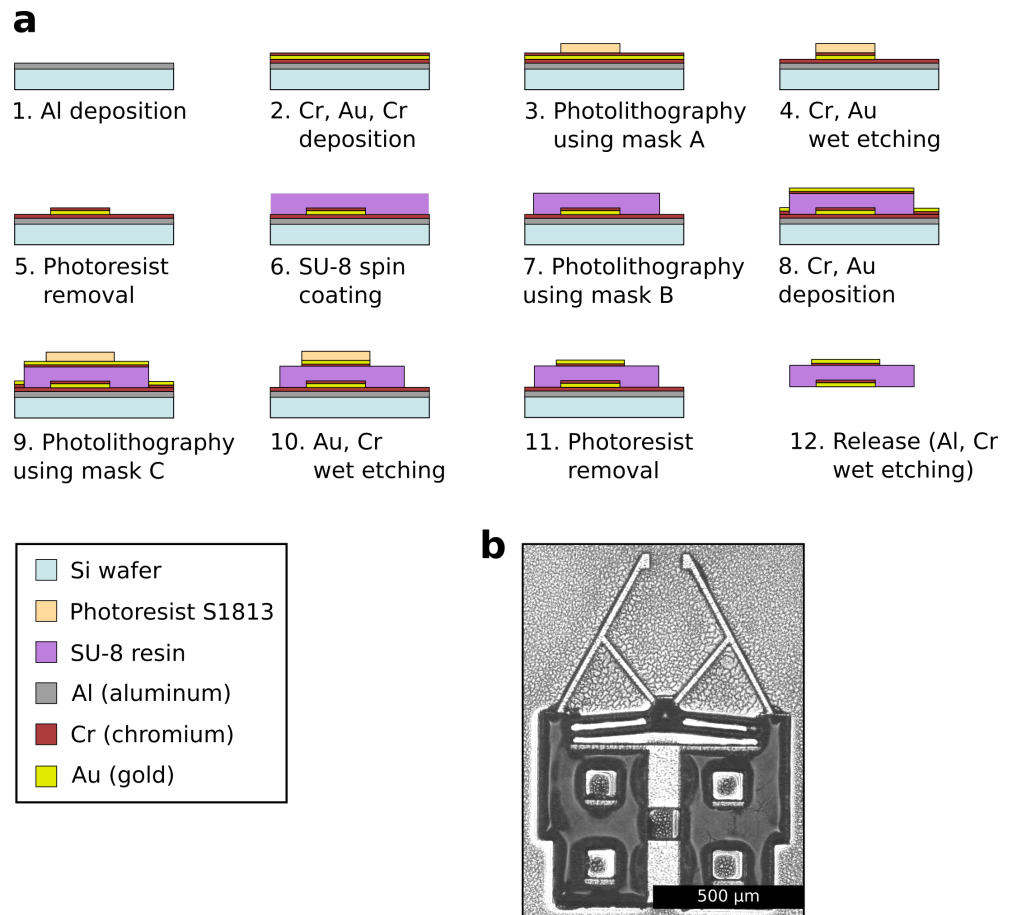


Figure 3. (a) Flowchart of the microgripper fabrication process. (1) Deposition of Al sacrificial layer. (2) Deposition of lower metallic layers. (3) First photolithography using mask A to shape the lower metallic layers. (4) Wet etching of lower metallic layers. (5) Removal of photoresist using acetone. (6) Spin coating of SU-8. (7) Second photolithography using mask B to shape the main body of the microgripper. (8) Deposition of upper metallic layers. (9) Third photolithography using mask C to shape the upper metallic layers. (10) Wet etching of upper metallic layers. (11) Removal of photoresist using acetone. (12) Wet etching of Al sacrificial layer and Cr layer to release the structures. (b) Image of a fabricated microgripper.

204 3. Experiments

205 In this section, the behavior of the fabricated microgrippers is characterized. The
206 optothermal response using laser actuation and the generated force of the microgrippers
207 are evaluated. Subsequently, the functionality of the microgrippers is confirmed through
208 a micromanipulation experiment of microbeads.

209 3.1. Microgripper Actuation and Response

210 In this section, the laser actuation of the microgripper by utilizing its optothermal
211 response is confirmed. The experimental setup for laser actuation of the microgripper is
212 shown in Figure 4(a). The system mainly consists of a CMOS camera (Allied Vision Inc.)
213 attached to a microscope to visualize and record the actuation of the microgripper. In
214 addition, a continuous wave (CW) laser (Oxxius Inc.) with a power of 53.3 mW and a
215 wavelength of 532.1 nm was used as a laser source. The laser beam was focused using
216 an 20× objective lens (Nikon Inc.), where the focused laser spot size was approximately
217 300 μm .

218
219 Figure 4(b) shows the actuation of the microgripper. The microgripper is initially in
220 a closed state without any laser heating. Upon laser heating of the chevron shuttle, the
221 open state of the microgripper can be realized. The initial gap between the two fingers
222 of the microgripper is approximately 100 μm (close) and then increased to 140 μm (open)
223 by laser heating. The achieved displacement of 40 μm is approximately 1.3 times higher
224 compared to similar designs without metallic layers deposition [17]. Figure 4(c) shows
225 the step response of the microgripper. From the response, a comparatively fast response
226 time, i.e. the time to reach 50% of the steady-state opening value of the microgripper, of
227 approximately 60 ms is confirmed, which is 23 times faster compared to similar designs
228 without metallic layers deposition [17]. Moreover, to confirm the frequency response
229 of the microgripper, the change in magnitude of the opening of the microgripper in
230 response to a frequency sweep is confirmed. Figure 4(d) shows the bode magnitude
231 plot of the microgripper response. The frequency sweep is achieved using a square
232 wave supplied to a tip/tilt mirror (Physics Instruments Inc.) to steer the laser beam
233 to and away from the chevron shuttle of the microgripper with frequencies ranging
234 from 1 to 20 Hz. As a result, the opening of the microgripper varied according to the
235 applied frequency. From the frequency response, a cut-off frequency, i.e. the frequency
236 where the magnitude reaches -3 dB value, is confirmed to be approximately 5.5 Hz. This
237 frequency modulated response can be used to apply a periodic force to grabbed cells
238 or microobjects in future work. These results clearly show the advantage of utilizing
239 metallic layer deposition to enhance optothermal actuation.

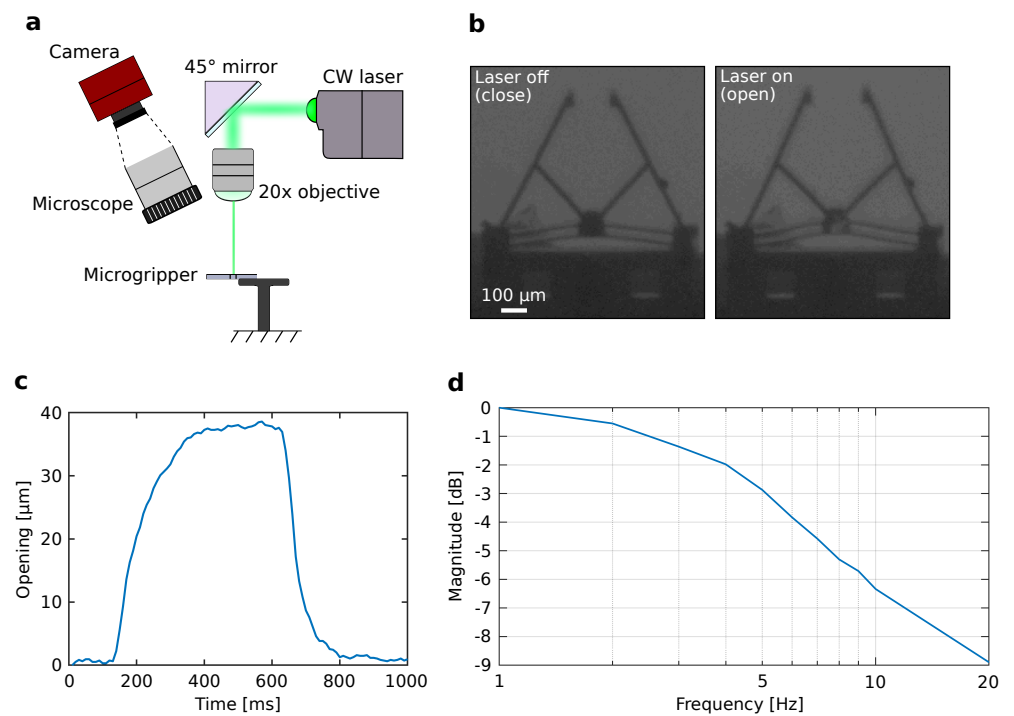


Figure 4. Laser actuation of the microgripper. (a) Experimental setup. (b) Experimental images showing the close and open states of the microgripper. (c) Step response of the microgripper. (d) Bode magnitude plot of the microgripper using a frequency sweep from 1 to 20 Hz

240 3.2. Generated Force

241 For micromanipulation applications, the gripping force generated by the micro-
 242 gripper should be suitable to firmly hold microobjects. Therefore, the force generated
 243 by the fingers of the microgripper is investigated. However, measuring the exact force
 244 generated by the two fingers connected to the chevron-shaped actuator proves to be chal-
 245 lenging, where a force sensing device should be placed between the fingers. Therefore,
 246 the stiffness of only one arm connected to the chevron-shaped actuator is confirmed,
 247 which gives a good estimate of the order of magnitude of the generated force. In fact,
 248 there are a number of design parameters that affects the generated force of the microgrip-
 249 per [17]. In this work, we investigate the effect of two parameters, namely the width of
 250 the chevron beams (W) and the number of chevron beams (n). The measurement setup
 251 is shown in Figure 5(a). A force sensor (Femtotoools inc.) with a resolution of $0.05 \mu\text{N}$
 252 and a range of $1000 \mu\text{N}$ is attached to a motorized x stage (Physik Instrumente Inc.) with
 253 a positioning accuracy of $0.05 \mu\text{m}$ and a range of 25 mm. The microgripper is attached to
 254 a stationary holder to have the same vertical position (z-axis) as the force sensor. The
 255 alignment between the probe of the force sensor and the finger of the microgripper is
 256 confirmed visually as shown in 5(b). Subsequently, the motorized x stage is moved for
 257 $20 \mu\text{m}$ to allow the probe to push the finger of the microgripper. A data acquisition
 258 routine is initiated simultaneously to record the position of the x stage and the force
 259 sensor data. Consequently, a linear relation between the force and the stage displacement
 260 can be obtained using linear regression, where the stiffness is confirmed as the slope
 261 of the plotted curve (please refer to Figure S1 in supplementary materials). It is worth
 262 noting that the force is applied along the x-axis; thus only one component of the force is
 263 present. Indeed, each finger of the microgripper has two degrees of freedom (x-axis and
 264 y-axis) and it is more accurate to describe the stiffness in a matrix form to account for the
 265 coupling stiffnesses. However, this increases the complexity of the force measurement
 266 experiment and the analysis. Therefore, as the aim is to get an estimate of the order of
 267 magnitude of the force applied by the microgripper to confirm its ability to manipulate
 268 microobjects, a simple unidirectional force estimation is sufficient. A more rigorous force

269 measurement will be planned in future work.

270

271 Figure 5(c-d) shows the experimental results, shown in blue bars, and simulation
272 results using Comsol, shown in brown bars, of the stiffness of one microgripper finger.
273 For the simulation, the commonly used value of 4 GPa for the Young's modulus of SU-8
274 is used [26]. The experimental measurements are repeated four times on four different
275 microgrippers for each plotted bar, where the error bars indicate the mean value and the
276 standard error of the measurements. Figure 5(c) shows the effect of the chevron beam
277 width on the stiffness. Two width values of 10 μm and 15 μm are investigated, where
278 the number of chevron beams is fixed to $n = 2$. It can be seen from the results that the
279 width of the chevron beam had a noticeable effect on the stiffness, where an increase in
280 stiffness of approximately 23% can be confirmed. Figure 5(d) shows the effect of the
281 number of chevron beams on the stiffness. Two cases with chevron-shaped actuators
282 having two, and four beams, respectively, were investigated, where the width of the
283 chevron beams are fixed to $W = 15 \mu\text{m}$. In this case, an increase of approximately 6% in
284 the stiffness when doubling the number of chevron beams can be confirmed. It can be
285 concluded from the figures that the impact on the stiffness is higher when increasing
286 the width of the chevron beams compared to increasing the number of chevron beams.
287 Finally, it can be noticed that the experimental results and the simulation results differ
288 significantly. This can be due to the difference in the Young's modulus value between
289 the simulation and experiments, since the physical parameters of SU-8 can change
290 according to the fabrication process. To confirm this effect, the Young's modulus was
291 increased in the simulation from 4 GPa to 8 GPa and the resulting stiffnesses are plotted
292 in Figures 5(c, d) shown in orange columns. It is found that by increasing the Young's
293 modulus, stiffness values that are much closer to the experimental results are obtained.
294 The residual difference between the experimental and simulation results can be caused
295 by the inaccuracies in the fabrication process, such as a drift in the width and thickness
296 of the chevron beams, or the alignment between the SU-8 layer and the gold layer. Still,
297 more investigation on the stiffness of SU-8 using our fabrication process will be planned
298 in future work. Overall, the experimental results serve as a good indicator for the order
299 of magnitude of the generated force, which is in the order of hundreds of micronewtons.
300 This force range is similar to many commercial microgrippers and is suitable for a variety
301 of micromanipulation applications [27].

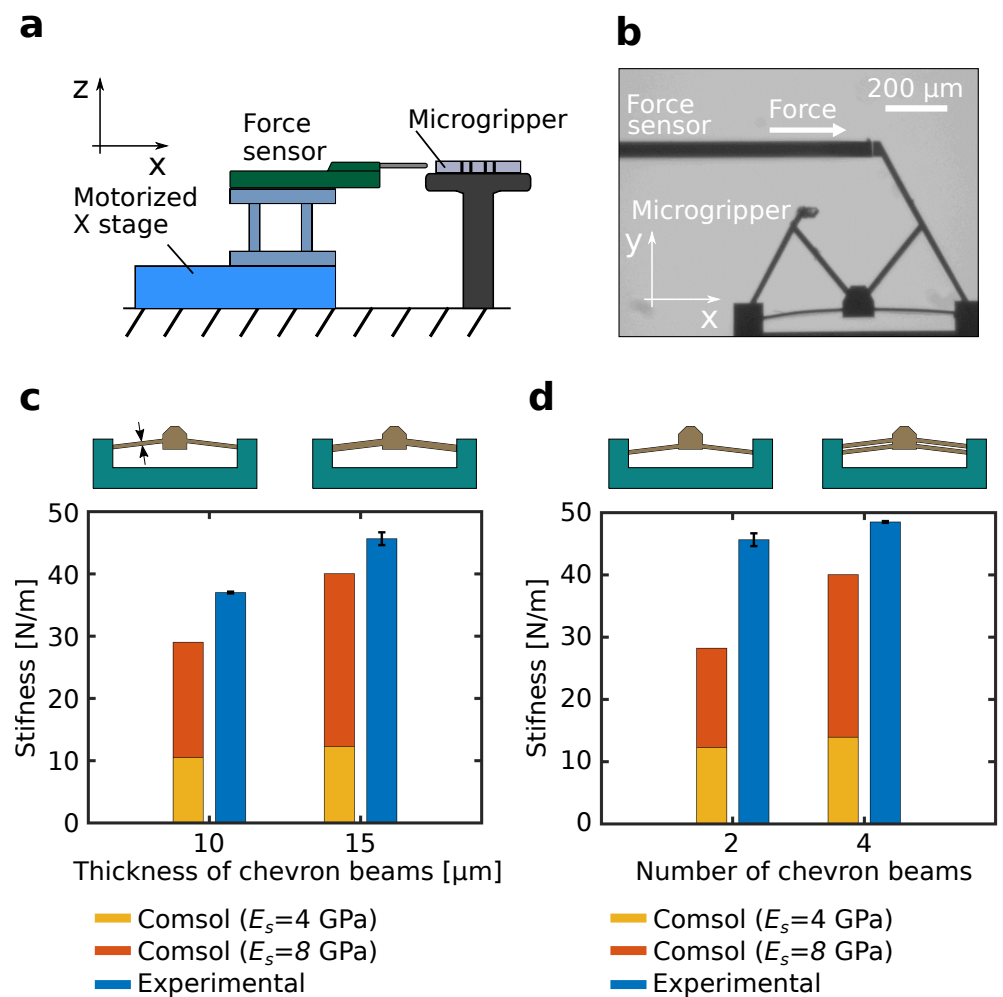


Figure 5. Force measurement of the microgripper. (a) Experimental setup. (b) Experimental image showing the alignment between the force sensor and a finger of the microgripper. (c) Effect of the width of the chevron beam on the stiffness. (d) Effect of the number of chevron beams on the stiffness. Blue bars show the experimental results. Orange bars and brown bars show the simulation results using SU-8 Young's moduli of 4 GPa and 8 GPa, respectively.

302 3.3. Application to Micromanipulation

303 To confirm the performance of the microgripper in micromanipulation applications,
 304 a pick-and-place experiment on a 120- μm diameter microbead is performed. The micro-
 305 gripper incorporates two pairs of chevron beams (four beams) to enhance the gripping
 306 force. The microbead is put on a cover glass and actuated using an XYZ piezoelectric
 307 motorized stage (Physik Instrumente Inc.), whereas the microgripper is attached to a
 308 stationary holder, as shown in Figure 6(a). The stationary position of the microgripper
 309 allows the initiation of open/close gripping motion at any instance during the experi-
 310 ment. Figure 6(b) demonstrate the results of the pick-and-place experiment. First, the
 311 microbead is brought to the same vertical position (z-axis) as the microgripper, where
 312 the microgripper is in a closed state with no application of laser heating (Figure 6(b-1)).
 313 Next, the microgripper is switched to an open state by initiating the laser heating, and
 314 the microbead is actuated and positioned between the arms of the gripper (6(b-2)). Con-
 315 sequently, the microgripper is returned to the closed state by switching off the laser and
 316 the microbead is firmly held and actuated away from the coverglass (6(b-3, b-4)). Finally,
 317 the opposite maneuver is repeated to place the microbead on the cover glass again (6(b-5,
 318 b-6)). The successful manipulation of the microbead demonstrates the potential of the
 319 proposed microgripper to be used in micromanipulation and biomedical applications.

320

321 To get a better conclusion on the weights of objects that can be manipulated using
 322 the microgripper, the weight of the manipulated microbead is estimated analytically.
 323 As the volume and density of the microbead are known, the weight is estimated to be
 324 approximately 1 μg . In fact, many microobjects fall in this range of size and density.
 325 Specifically, biological cells are mostly equal or smaller than 120 μm in diameter with
 326 lower densities than glass. Therefore, the proposed microgripper is expected to be able
 327 to handle a large variety of microobjects including cells. The maximum weight limitation
 328 of the gripped object is mainly affected by the static friction force generated by the
 329 normal force applied on the object. This requires the estimation of the static friction
 330 coefficient, which is challenging to acquire at this small scale. Nonetheless, the generated
 331 force of the microgripper in the range of hundreds of μN is similar to many commercial
 332 microgrippers and is suitable for many micromanipulation applications.

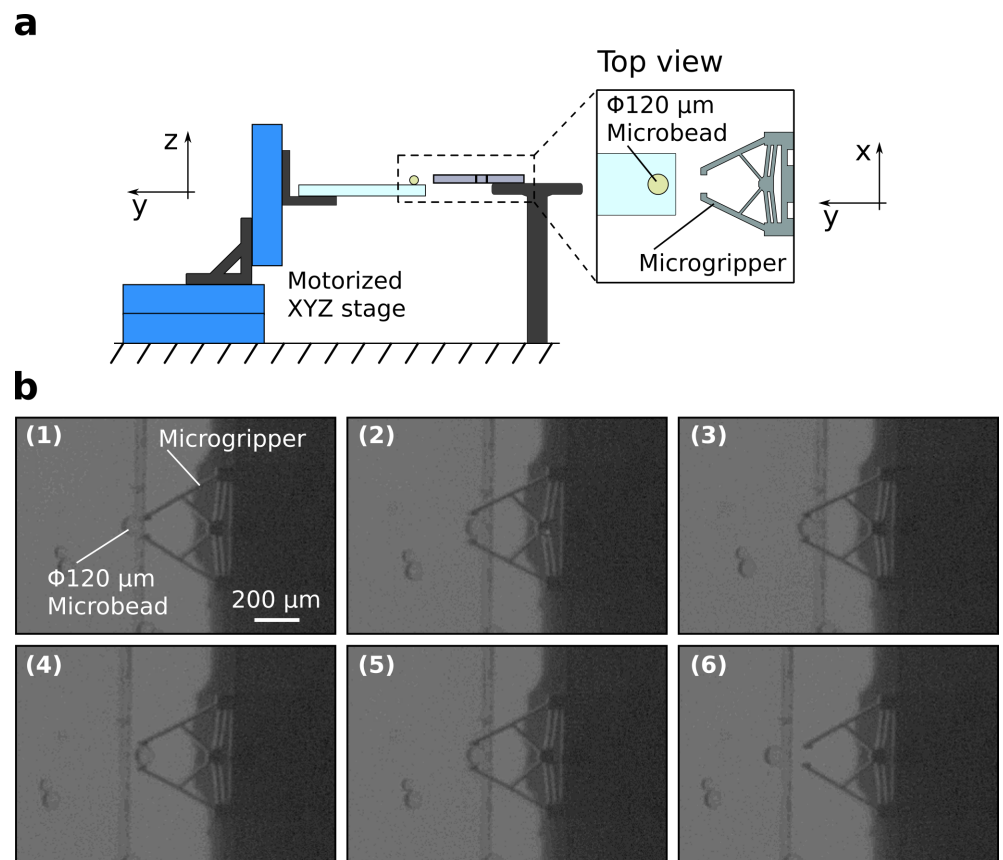


Figure 6. Pick-and-place of a microbead. (a) Experimental setup. (b) Snapshots of the experiment showing the successful pick-and-place of a 120- μm diameter microbead on a cover glass. See attached video.

333 4. Conclusions

334 In this article, we proposed a laser actuated microgripper based on a metal-coated
 335 chevron-shaped actuator for micromanipulation applications. The thermomechanical
 336 model of the metal-coated microgripper was established to identify the parameters affect-
 337 ing its thermal deflection. Consequently, an optimization process was conducted to find
 338 the optimal thickness of the metallic layer that achieves the largest possible deflection.
 339 Microgrippers were fabricated with SU-8 resin and gold coating using conventional
 340 photolithography and metal deposition techniques. The optothermal response and the
 341 generated force of the microgrippers were verified through characterization experiments.
 342 The microgrippers could realize a relatively large opening of 40 μm with a relatively fast
 343 response time of 60 ms. Finally, the functionality of the microgripper was demonstrated

344 through a successful pick-and-place experiment of a microbead.

345

346 Because this kind of remotely actuated microgrippers are highly promising for
347 mobile microrobotic application, the future direction of this work is to utilize the micro-
348 gripper as a mobile microrobot to be deployed in lab-on-chip applications. To achieve
349 this goal, the behavior of the optothermal actuation in liquid needs to be verified first. In
350 addition, a remote actuation scheme, such as magnetic or acoustic actuation, to control
351 the position of the microgripper needs to be integrated and tested. Moreover, as the
352 fluidic flows generated by objects inside microfluids are significant and can affect the
353 position of target microobjects, it is desirable to reduced the footprint of the microgripper
354 by fabricating a miniaturized version. In this case, the size of the laser spot needs to be
355 adjusted to be compatible with the miniaturized chevron-shaped actuator.

356 **Author Contributions:** Conceptualization, H.C., P.T. and A.B.; software, B.A., H.C., P.T. and A.B.;
357 formal analysis, B.A., H.C., P.T. and A.B.; writing, B.A. and A.B.; supervision, A.B.; funding
358 acquisition, A.B. All authors have read and agreed to the submitted version of the manuscript.

359 **Funding:** This work was supported in part by the EIPHI Graduate School under Contract ANR-
360 17-EURE-0002, in part by the MiMedi project funded by BPI France under Grant DOS0060162/00,
361 and by the European Union through the European Regional Development Fund of the Region
362 Bourgogne-Franche-Comté under Grant FC0013440, in part by the French ROBOTEX network and
363 its FEMTO-ST technological facility under Grant ANR-10-EQPX-44-01, and in part by the french
364 RENATECH network and its FEMTO-ST technological facility.

365 **Conflicts of Interest:** The authors declare no conflict of interest.

References

1. Zhang, Z.; Wang, X.; Liu, J.; Dai, C.; Sun, Y. Robotic micromanipulation: Fundamentals and applications. *Annual Review of Control, Robotics, and Autonomous Systems* **2019**, *2*, 181–203.
2. Li, X.; Fukuda, T. Magnetically guided micromanipulation of magnetic microrobots for accurate creation of artistic patterns in liquid environment. *Micromachines* **2020**, *11*, 697.
3. Jing, W.; Chowdhury, S.; Guix, M.; Wang, J.; An, Z.; Johnson, B.V.; Cappelleri, D.J. A microforce-sensing mobile microrobot for automated micromanipulation tasks. *IEEE Transactions on Automation Science and Engineering* **2018**, *16*, 518–530.
4. Gursky, B.; Bütetisch, S.; Leester-Schädel, M.; Li, K.; Matheis, B.; Dietzel, A. A disposable pneumatic microgripper for cell manipulation with image-based force sensing. *Micromachines* **2019**, *10*, 707.
5. Power, M.; Thompson, A.J.; Anastasova, S.; Yang, G.Z. A monolithic force-sensitive 3D microgripper fabricated on the tip of an optical fiber using 2-photon polymerization. *Small* **2018**, *14*, 1703964.
6. Yin, C.; Wei, F.; Zhan, Z.; Zheng, J.; Yao, L.; Yang, W.; Li, M. Untethered microgripper-the dexterous hand at microscale. *Biomedical microdevices* **2019**, *21*, 82.
7. Velosa-Moncada, L.A.; Aguilera-Cortés, L.A.; González-Palacios, M.A.; Raskin, J.P.; Herrera-May, A.L. Design of a novel MEMS microgripper with rotatory electrostatic comb-drive actuators for biomedical applications. *Sensors* **2018**, *18*, 1664.
8. Lyu, Z.; Xu, Q. Recent design and development of piezoelectric-actuated compliant microgrippers: A review. *Sensors and Actuators A: Physical* **2021**, *331*, 113002.
9. Cauchi, M.; Grech, I.; Mallia, B.; Mollicone, P.; Sammut, N. The effects of cold arm width and metal deposition on the performance of a U-beam electrothermal MEMS microgripper for biomedical applications. *Micromachines* **2019**, *10*, 167.
10. Kuo, J.C.; Huang, H.W.; Tung, S.W.; Yang, Y.J. A hydrogel-based intravascular microgripper manipulated using magnetic fields. *Sensors and Actuators A: Physical* **2014**, *211*, 121–130.
11. Pevec, S.; Donlagic, D. Optically controlled fiber-optic micro-gripper for sub-millimeter objects. *Optics letters* **2019**, *44*, 2177–2180.
12. Ahmad, B.; Gauthier, M.; Laurent, G.J.; Bolopion, A. Mobile Microrobots for In Vitro Biomedical Applications: A Survey. *IEEE Transactions on Robotics* **2021**. doi:10.1109/TRO.2021.3085245.
13. Feng, L.; Hagiwara, M.; Ichikawa, A.; Arai, F. On-chip enucleation of bovine oocytes using microrobot-assisted flow-speed control. *Micromachines* **2013**, *4*, 272–285.
14. Ahmad, B.; Kawahara, T.; Yasuda, T.; Arai, F. Microrobotic platform for mechanical stimulation of swimming microorganism on a chip. IEEE/RSJ International Conference on Intelligent Robots and Systems. Chicago, IL USA, 2014, pp. 4680–4685.
15. Villangca, M.J.; Palima, D.; Banas, A.R.; Glückstad, J. Light-driven micro-tool equipped with a syringe function. *Light: Science & Applications* **2016**, *5*, e16148.
16. Huang, C.; Lv, J.a.; Tian, X.; Wang, Y.; Liu, J.; Yu, Y. A remotely driven and controlled micro-gripper fabricated from light-induced deformation smart material. *Smart Materials and Structures* **2016**, *25*, 095009.

17. Elbuken, C.; Khamesee, M.B.; Yavuz, M. Design and implementation of a micromanipulation system using a magnetically levitated MEMS robot. *IEEE/ASME Transactions on Mechatronics* **2009**, *14*, 434–445.
18. Lu, X.; Zhang, H.; Fei, G.; Yu, B.; Tong, X.; Xia, H.; Zhao, Y. Liquid-crystalline dynamic networks doped with gold nanorods showing enhanced photocontrol of actuation. *Advanced Materials* **2018**, *30*, 1706597.
19. Lahikainen, M.; Zeng, H.; Priimagi, A. Reconfigurable photoactuator through synergistic use of photochemical and photothermal effects. *Nature communications* **2018**, *9*, 1–8.
20. Shivhare, P.; Uma, G.; Umapathy, M. Design enhancement of a chevron electrothermally actuated microgripper for improved gripping performance. *Microsystem Technologies* **2016**, *22*, 2623–2631.
21. Sharif, M.; Pourabbas, B.; Sangermano, M.; Sadeghi Moghadam, F.; Mohammadi, M.; Roppolo, I.; Fazli, A. The effect of graphene oxide on UV curing kinetics and properties of SU8 nanocomposites. *Polymer International* **2017**, *66*, 405–417.
22. Ge, F.; Lu, X.; Xiang, J.; Tong, X.; Zhao, Y. An optical actuator based on gold-nanoparticle-containing temperature-memory semicrystalline polymers. *Angewandte Chemie* **2017**, *129*, 6222–6226.
23. Bagheri, M.; Chae, I.; Lee, D.; Kim, S.; Thundat, T. Selective detection of physisorbed hydrocarbons using photothermal cantilever deflection spectroscopy. *Sensors and Actuators B: Chemical* **2014**, *191*, 765–769.
24. Wang, Y.; Li, M.; Chang, J.K.; Aurelio, D.; Li, W.; Kim, B.J.; Kim, J.H.; Liscidini, M.; Rogers, J.A.; Omenetto, F.G. Light-activated shape morphing and light-tracking materials using biopolymer-based programmable photonic nanostructures. *Nature communications* **2021**, *12*, 1–9.
25. Sangermano, M.; Calvara, L.; Chiavazzo, E.; Ventola, L.; Asinari, P.; Mittal, V.; Rizzoli, R.; Ortolani, L.; Morandi, V. Enhancement of electrical and thermal conductivity of Su-8 photocrosslinked coatings containing graphene. *Progress in Organic Coatings* **2015**, *86*, 143–146.
26. Xu, T.; Yoo, J.H.; Babu, S.; Roy, S.; Lee, J.B.; Lu, H. Characterization of the mechanical behavior of SU-8 at microscale by viscoelastic analysis. *Journal of Micromechanics and Microengineering* **2016**, *26*, 105001.
27. Kim, K.; Liu, X.; Zhang, Y.; Sun, Y. Micronewton force-controlled manipulation of biomaterials using a monolithic MEMS microgripper with two-axis force feedback. IEEE International Conference on Robotics and Automation. Pasadena, CA USA, 2008, pp. 3100–3105.